Reprinted from

JAPANESE JOURNAL OF
APPLIED
PHYSICS

REGULAR PAPER

Improvement of Automated Identification of the Heart Wall in Echocardiography by Suppressing Clutter Component

Hiroki Takahashi, Hideyuki Hasegawa, and Hiroshi Kanai

Jpn. J. Appl. Phys. **52** (2013) 07HF17

Japanese Journal of Applied Physics **52** (2013) 07HF17 **REGULAR PAPER**
http://dx.doi.org/**10.7567/JJAP.52.07HF17**

Improvement of Automated Identification of the Heart Wall in Echocardiography by Suppressing Clutter Component

Hiroki Takahashi[1], Hideyuki Hasegawa[1,2], and Hiroshi Kanai[2,1]

[1]*Graduate School of Biomedical Engineering, Tohoku University, Sendai 980-8579, Japan*
[2]*Graduate School of Engineering, Tohoku University, Sendai 980-8579, Japan*
E-mail: htaka@us.ecei.tohoku.ac.jp

Received November 21, 2012; accepted March 27, 2013; published online July 22, 2013

For the facilitation of analysis and elimination of the operator dependence in estimating the myocardial function in echocardiography, we have previously developed a method for automated identification of the heart wall. However, there are misclassified regions because the magnitude-squared coherence (MSC) function of echo signals, which is one of the features in the previous method, is sensitively affected by the clutter components such as multiple reflection and off-axis echo from external tissue or the nearby myocardium. The objective of the present study is to improve the performance of automated identification of the heart wall. For this purpose, we proposed a method to suppress the effect of the clutter components on the MSC of echo signals by applying an adaptive moving target indicator (MTI) filter to echo signals. In vivo experimental results showed that the misclassified regions were significantly reduced using our proposed method in the longitudinal axis view of the heart.

1. Introduction

Echocardiography is the predominant modality for the early detection of cardiac diseases because of its low cost, noninvasiveness, and high temporal resolution. Myocardial ischemia, which occurs upon a mismatch between the coronary blood flow and myocardial metabolism, decreases myocardial contraction and relaxation. Methods for measuring of myocardial motion and deformation (i.e., myocardial strain) using echocardiography are very useful to find out regional myocardial abnormalities, such as dysfunction in contraction and relaxation, caused by myocardial ischemia.[1,2)] The myocardial motion and strain rate, which is equivalent to the shortening velocity per initial muscle length, can be quantitatively evaluated in echocardiography by the ultrasonic Doppler shift or speckle motion.[3–7)] The systolic velocity of an ischemic myocardium tends to be lower than that of a normal myocardium.[8,9)] The systolic strain rate in myocardial ischemia is also reduced, and, also, the myocardial strain and strain rate have the advantage of being less influenced by the tethering effect from adjacent tissue.[10)] By estimating the myocardial strain rate, it is possible to observe post-systolic shortening, which is sensitive to myocardial ischemia under dobutamine stress.[11)] On the other hand, it is reported that the temporal change in the amplitude of an echo signal backscattered from the myocardium is in good agreement with the rate of change in the thickness of the myocardium and has the possibility of being used to estimate of myocardial deformation resulting from myocardial contraction and relaxation.[12)] Furthermore, the propagation of electrical excitation and mechanical vibration in the cardiac wall has been noninvasively measured in echocardiography to detect regional tissue damage, which is involved in ischemia and arrhythmia.[13–15)] In most estimates of the myocardial function as presented above, the myocardium, which is the object to be analyzed, needs to be manually identified by an operator. However, this task is very time-consuming and suffers from inter- and intraobserver variability. For the facilitation of analysis and the elimination of operator dependence, automated identification of the heart wall needs to be realized.

Automated (or semi-automated) methods for segmenting the left ventricle (LV) in echocardiographic images have been proposed by extracting the boundary of the LV boundary between the left ventricular walls and the lumen.[16–19)] Segmentation methods for the LV can be used to calculate diagnostic indexes, such as the cardiac chamber size and ejection fraction, related to the global cardiac function. These methods, however, cannot be applied to obtain parameters of myocardial functions, such as the myocardial strain rate, because the myocardia in the LV chamber are not identified. Identification of the myocardia composing heart walls is a challenging task because of the low echogenicity in the myocardium, the low contrast, and dropout.

We have developed a method for automated identification of the heart wall regions, which include the myocardia, throughout an entire cardiac cycle by tracking the points identified as the heart wall in an initial frame.[20)] In our method, multiple features, such as echogenicity and temporal changes in the phases of echo signals, are extracted to accurately identify the heart wall in the initial frame. Echo signals in transthoracic echocardiography contain undesirable stationary clutter which is caused by the echoes from external tissue such as the ribs.[21,22)] In our previous study,[20)] to reduce this stationary clutter, high-pass filtering, corresponding to moving target indicator (MTI) filtering,[23)] was applied to RF signals before extracting features. However, the magnitude-squared coherence (MSC) function of echo signals,[20,22)] which is one of the features, is still affected by undesirable echoes. This remaining clutter increases the MSC in the cardiac lumen (essentially, the MSC in the cardiac lumen is expected to be low) and causes misclassified regions. In the present study, we investigated the source of clutter, which increases the MSC in the cardiac lumen, and suppressed the influence of this clutter by adaptively determining the frequency response of an MTI filter.

2. Estimation of Magnitude-Squared Coherence Function with Tracking Method

Using a feature such as the echogenicity, which depends only on the echo amplitude, the heart wall is not completely

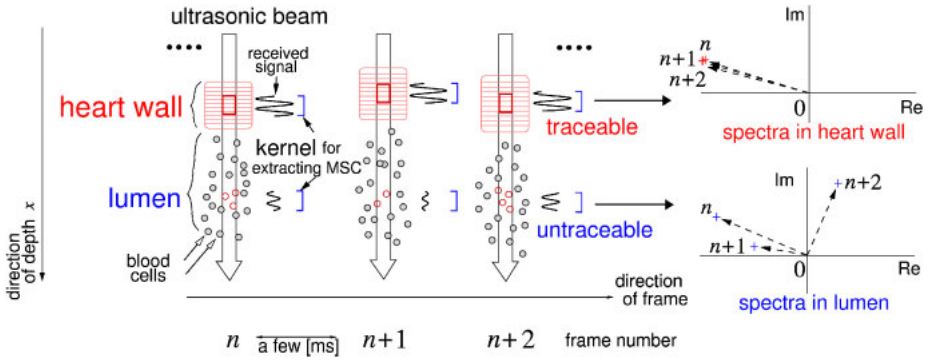

Fig. 1. (Color online) Illustration of changes in waveforms of echo signals in kernel.

distinguished from the lumen because there is also a region with low echo amplitude inside the heart wall region. Thus, additional second and third features, which can evaluate differences in echo signals between the heart wall and the lumen regardless of the echo amplitude, were adopted to accurately classify the region with low echo amplitude inside the heart wall region. In this study, the MSC function estimated by the *phased tracking method*[24] and the temporal phase shift of echo signals are used as second and third features, respectively.[20]

In the ultrasonic echo signal measured at a high frame rate the motion of the heart wall can be tracked accurately by the phased tracking method. On the other hand, as shown in Fig. 1, blood cells in the cardiac lumen are difficult to track because they slip away from the focal area of the ultrasonic beam owing to blood flow. The temporal changes in phases of echo signals in the kernel caused by the global motion of the heart wall are compensated because the echo signal is only time-shifted while the waveform of the echo from the lumen changes significantly owing to the large change in the relative locations of scatterers. Therefore, there is a significant difference in the temporal changes in the waveforms of ultrasonic echoes in an assigned kernel, in which the motion of the tissue is estimated using the phased tracking method, between the heart wall and lumen regions. The displacement $u_x(n+k)$ between the nth and $(n+k)$th frames of tissue in a kernel assigned around depth x in the nth frame is estimated by the phased tracking method. The complex spectrum, $Y(f;\hat{x}(n+k);(n+k))$, of the RF echo signal in the kernel at the position $\hat{x}(n+k)$ $[= x + u_x(n+k)]$ in the $(n+k)$th frame is obtained by applying the discrete Fourier transform (DFT) to the RF echo signal in the kernel. Using the complex spectra $\{Y(f;\hat{x}(n+k);n+k)\}$, the characteristics of phase changes in echoes in the kernel between two consecutive frames, which depend on the motion and the deformation of an object, are evaluated by the MSC function,[20,22] $|\gamma(f;x;n)|^2$, at a scan line in the nth frame as follows:

$$|\gamma(f;x;n)|^2 = \frac{|\mathrm{E}_k[Y(f;\hat{x}(n+k);n+k)^* Y(f;\hat{x}(n+k+1);n+k+1)]|^2}{\mathrm{E}_k[|Y(f;\hat{x}(n+k);n+k)|^2]\mathrm{E}_k[|Y(f;\hat{x}(n+k+1);n+k+1)|^2]}, \quad (1)$$

where $\mathrm{E}_k[\cdot]$ and * denote the time averaging (for 50 frames) and complex conjugate, respectively. The numerator of Eq. (1) denotes the power of time-averaged complex cross spectra, which evaluate the variation of temporal changes in phases of the complex spectra between two frames. The denominator of Eq. (1) denotes the average power of the complex spectra. Thus, the value of Eq. (1) does not depend on the echo amplitude. In this study, the MSC at a frequency, f, of 4.4 MHz, which was higher than the transmission frequency of 3.75 MHz, was used to obtain a high contrast between the heart wall and lumen.[22] Conventionally, the MSC and the echogenicity are extracted from the echo signal filtered with a high-pass filter whose cutoff frequency is 10 Hz (around DC) to reduce the effects of echoes from stationary structures.

3. Investigation of Source of Clutter

A modified diagnostic ultrasound system (Aloka α-10) with a 3.75 MHz phased array probe was used for the experiments in this study. This system was modified to acquire individual RF echo signals received by 96 elements. Parallel beamforming[25,26] and spatial compounding were applied in off-line processing using RF echo signals measured by elements. Plane waves were transmitted in seven directions at angle intervals of 6°, and 16 receiving beams were formed at angle intervals of 0.375° in each transmission by parallel beamforming.[27] Beamformed RF echo signals sampled at 15 MHz were spatially compounded to reduce discontinuities in the ultrasound image. The number of compoundings was determined by the transmission aperture width projected in the transmission direction.[27] Figure 2(a) illustrates the relationship between the projected transmission aperture width l_w and the angular width of the projected transmission aperture, θ_w; in the present study, l_w was equal to $L\cos\phi$, where L and ϕ are the width of the transmission aperture and the transmission beam steering angle, respectively, in plane wave transmission. Figure 2(b) illustrates an example in the case of three compounding at a point of interest **p**. A beamformed RF signal was compounded to obtain a compounded RF signal at **p** when the angular difference between the direction of transmission, from which the beamformed RF signal was obtained, and that of a point of interest **p** (the origin corresponds to the center of the transmission aperture) was less than twice the angular width

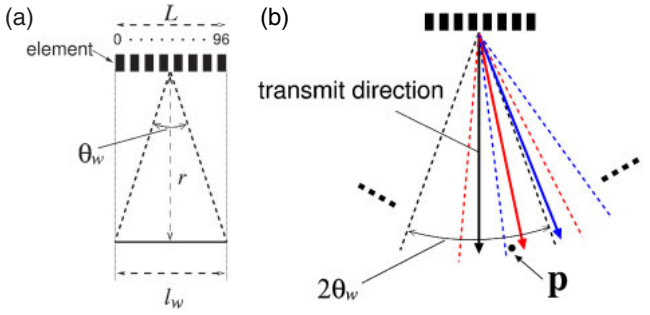

Fig. 2. (Color online) Illustrations of (a) projected transmit aperture width l_w and (b) compounding procedure at a point of interest **p** in the case of the number of compounding of 3 with plane wave transmission (black, red, and blue dashed lines show angular width θ_w at **p** in three successive transmission).

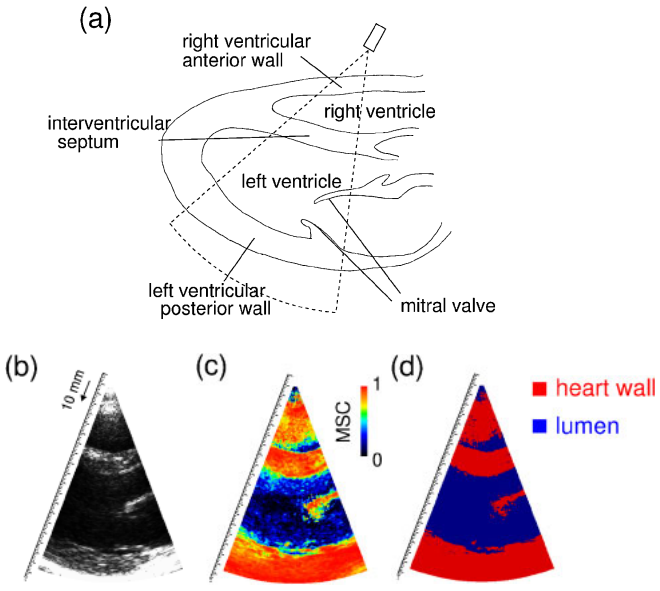

Fig. 3. (Color online) (a) Acquisition area of beamformed RF echo signals, (b) B-mode image, (c) spatial distribution of MSCs obtained with previously determined MTI filter whose cutoff frequency was set at 10 Hz, and (d) region-identified image obtained by feature classification using EM algorithm.[20)]

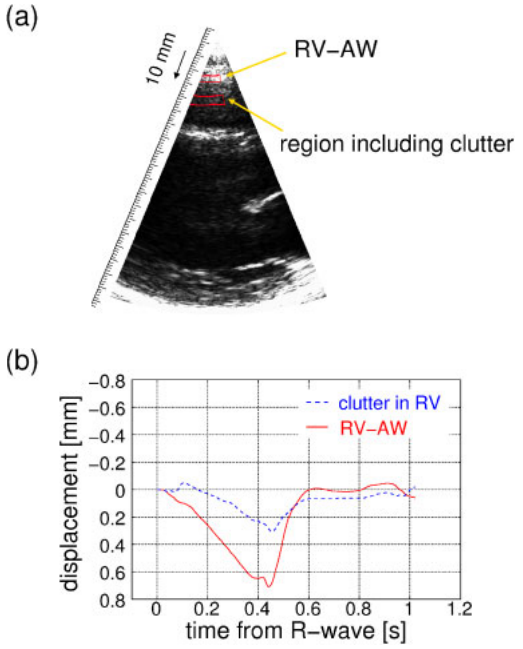

Fig. 4. (Color online) Motion of RV-AW, and clutter in RV with high MSC estimated by the phased tracking method. (a) Regions assigned in RV-AW and in RV. (b) Waveforms of spatial means of displacements in these regions measured by the phased tracking method.

of the projected transmission aperture, $2\theta_w$.[27)] As shown in Fig. 2(a), the angular width θ_w varied with the distance between the point of interest **p** and the center of the transmission aperture r and the projected aperture width l_w. Therefore, the number of compoundings was also changed depending on the position of **p**. The total number of transmissions was from one (no compounding) to seven in this in vivo experiment. The heart of a 23-year-old male was measured in the longitudinal axis view at a very high frame rate of 860 Hz using parallel beamforming with plane wave transmission. Figures 3(a) and 3(b) respectively show the acquisition area of the beamformed RF echo signals and the B-mode image, which was constructed by detecting envelopes in beamformed RF signals sampled at 15 MHz. Figure 3(c) shows the spatial distribution of the MSC obtained with a previously determined MTI filter, whose cutoff frequency is 10 Hz (around DC). As shown in Fig. 3(c), the MSC in the right ventricle (RV) is as high as that in the heart wall regions, while the echogenicity in the RV is low compared with that in the heart wall regions. Figure 3(d) shows a region-identified image by feature classification obtained using the expectation-maximization (EM) algorithm,[28)] in which there are misclassified regions caused by the high MSC in the RV.

We investigated the source of this clutter, which increases the MSC in the cardiac lumen, to propose a method for suppressing it. Figure 4 shows the motion of the right ventricular anterior wall (RV-AW) and the clutter in the RV with the high MSC estimated with the phased tracking method.[24)] The displacement waveforms shown in Fig. 4(b) were spatially averaged inside the regions surrounded by red lines in Fig. 4(a). As shown in Fig. 4(b), the clutter in the RV exhibits the motion similar to that in the RV-AW. Lediju et al. also reported that clutter in the ventricle has motion similar to that in the nearby myocardium.[29)] The MSC in the cardiac lumen can be increased by multiple reflection and off-axis echo (echo from an off-axis object caused by a mainlobe or the sidelobe) from the nearby myocardium in addition to extra cardiac structures, such as ribs and lungs. Therefore, the clutter in the cardiac lumen is found not to be suppressed completely by the previously determined MTI filter which suppresses the effect of echoes from stationary structures.

4. Principle

4.1 Clutter reduction in coherence estimation

Well-suitable MTI filtering has the potential to suppress the increase in the MSC caused by clutter in the cardiac lumen and to preserve the MSC in the heart wall in the case when the power of the clutter component in the cardiac lumen is lower than the power of the echo from the heart wall. That is the reason why the MSC in the cardiac lumen does not

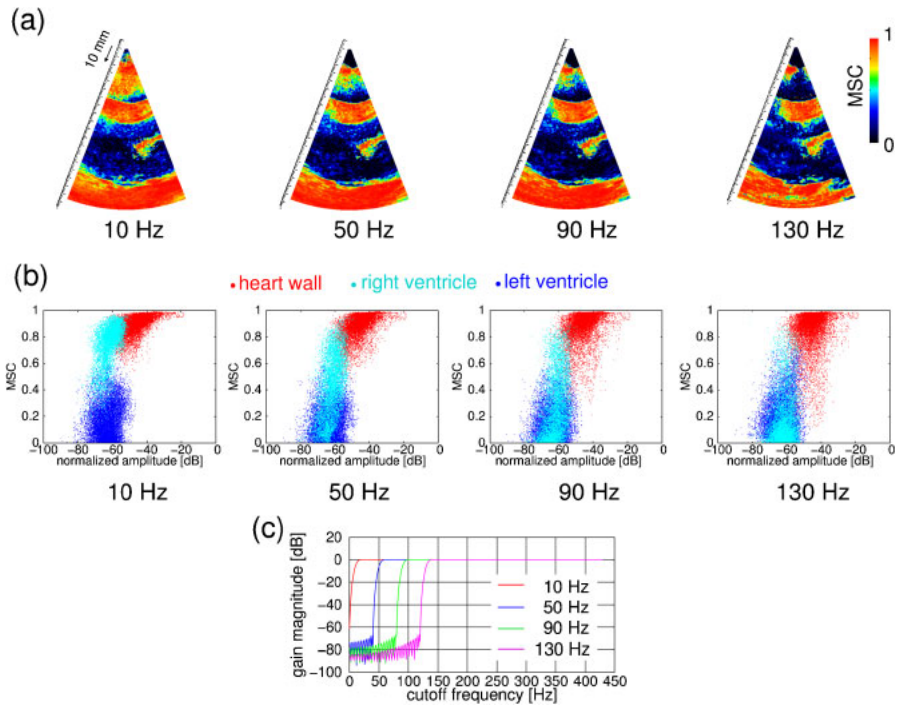

Fig. 5. (Color online) (a) Spatial distributions of MSCs, (b) distributions of features in feature space (echogenicity vs MSC) indicated by red points (heart wall), cyan points (RV), and blue points (LV) at different cutoff frequencies of MTI filter. (c) Frequency responses of MTI filters used in (a) and (b).

depend on the powers (amplitudes) but depends on the temporal changes in the phases of echo signals.

Figures 5(a) and 5(b) show the spatial distributions of the MSCs and the distributions of the features in the feature space (echogenicity vs MSC), respectively, in manually assigned regions at several cutoff frequencies of the MTI filter (FIR high-pass filter) at the beginning of the slow filling phase.[20] The distributions of the features of the manually assigned region in the heart wall [interventricular septum (IVS) and left ventricular posterior wall (LV-PW)], RV, and LV are shown as red, cyan, and blue points in Fig. 4(b), respectively. Figure 5(c) shows the frequency responses of the MTI filters used in Figs. 5(a) and 5(b), where the filters' impulse responses have the same length. The sinc function multiplied by the Kaiser window was used as the impulse response of the MTI filter. As shown in Fig. 5(a), the regions with the high MSC in the RV were decreased in intensity and the MSCs in the heart walls were still high when the cutoff frequency of the MTI filter was set to 50 Hz. On the other hand, as shown in Fig. 5(b), it was found that the region with the clutter in the RV cannot be distinguished from the region with the low echogenicity in the heart walls using the previously determined MTI filter which suppresses the clutter caused by echoes from only stationary structures. The result shows that the increase in the MSC caused by clutter can be suppressed while preserving a high MSC in the heart wall by adjusting the cutoff frequency of the MTI filter.

4.2 Adaptive determination of MTI filter response

In the present study, we proposed a method for suppressing of the effect of clutter in the MSC estimation to improve automated identification of the heart wall. This proposed method estimates the cutoff frequency of the MTI filter at which the MSCs in the heart wall region start to be critically decreased, to suppress the effect of the clutter component in the lumen while preserving a high MSC in the heart wall. First, candidate points in the heart wall region are extracted on the basis of the echo amplitudes in manually assigned areas. The candidate points have echo amplitudes between e_1 and e_2. The upper limit amplitude, e_2, is set to the amplitude at which the cumulative probability of the Rayleigh distribution fitted to the measured histogram [the empirical probability density function (PDF)] of the echo amplitudes in the assigned area in the heart wall is 95%. The lower limit amplitude, e_1, is set to the higher value of either the expectation amplitude, $e_{\mathrm{exp},1}$, of the Rayleigh distribution fitted to the empirical PDF of the echo amplitudes in the heart wall or the amplitude, $e_{\mathrm{cum},1}$, at which the cumulative probability of the Rayleigh distribution fitted to the empirical PDF of the echo amplitudes in the lumen is 95%. This is why it is undesirable for the candidate points of the heart wall region to be selected from the lumen region in the case when the expectation amplitude in the assigned area inside the heart wall, $e_{\mathrm{exp},1}$, is very low. Next, the spatial mean $\mu(f_p(i))$ and the standard error of the mean $\varepsilon(f_p(i))$, which corresponds to the standard deviation divided by the square root of the number of points, of the MSCs of candidate points are calculated while the cutoff frequency, $f_p(i)$, of the MTI filter is gradually increased from f_s (around DC) at a pitch of df_p as follows:

$$f_p(i) = f_s + i \cdot df_p \quad (i = 0, 1, \ldots, N). \tag{2}$$

In the present study, both f_s and df_p are set to 10 Hz. Next, the spatial mean $\mu(f_p(i))$ and the standard error of the mean $\varepsilon(f_p(i))$ are divided into group 1 with $\{f_p(m)\}$ $(m = 0, 1, \ldots, N_t)$ and group 2 with $\{f_p(n)\}$ $(n = N_t + 1, \ldots, N)$ by a threshold $f_p(N_t)$ $(0 < N_t < N)$. After that, the slope a_j

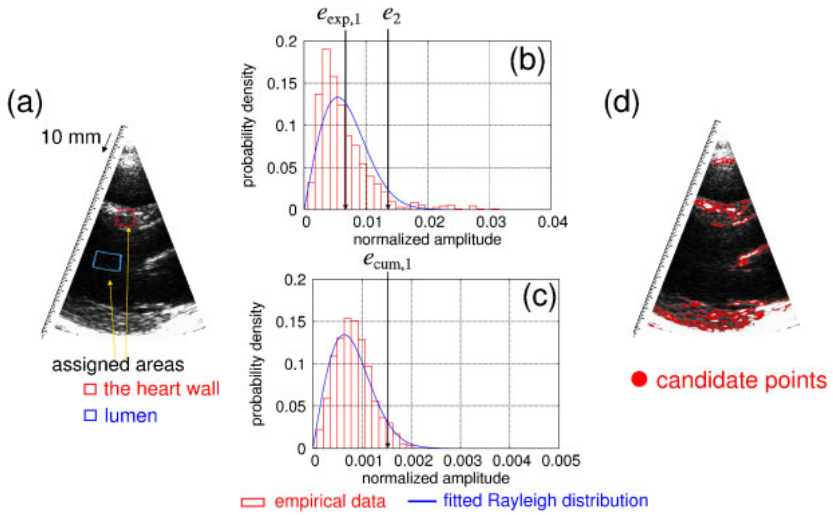

Fig. 6. (Color online) (a) Regions manually assigned for determination of frequency response of MTI filter and initial parameters of EM algorithm. Histograms of echo amplitudes and fitted Rayleigh distributions in regions assigned in (b) heart wall and (c) lumen regions shown in (a). (d) Candidate points for the heart wall extracted on the basis of echo amplitudes in the assigned regions.

and intercept b_j of the regression line with respect to each group j ($\in \{0, 1\}$) are estimated using the weighted least-squares method, which minimizes the weighted residual sum of squares E_j. The weighted residual sum of squares, E_j, for each group j is defined as follows:

$$E_1 = \frac{1}{N_t + 1} \sum_{i=0}^{N_t} \frac{(\mu(f_p(i)) - a_1 f_p(i) - b_1)^2}{\varepsilon^2(f_p(i))}, \quad (3)$$

$$E_2 = \frac{1}{N - N_t} \sum_{i=N_t+1}^{N} \frac{(\mu(f_p(i)) - a_2 f_p(i) - b_2)^2}{\varepsilon^2(f_p(i))}. \quad (4)$$

The minimum of E_j, which is estimated by the weighted least-squares method for each group j, is defined as $E_{\min,j}(N_t)$ at different thresholds $f_p(N_t)$. In group 1, the intercept of the regression line, b_1, is estimated by the weighted least-squares method where the slope, a_1, is zero because the MSCs in the heart wall are expected not to change in the case when the cutoff frequency of the MTI filter is in group 1 (low cutoff frequency). The total of the residual sum of squares for the two groups, $E(N_t)$, is defined as follows:

$$E(N_t) = E_{\min,1}(N_t) + E_{\min,2}(N_t). \quad (5)$$

The total errors $\{E(N_t)\}$ are calculated at different thresholds $f_p(N_t)$. Finally, the cutoff frequency of the MTI filter is determined as the frequency where two regression lines at the minimum total error intersect. The MSC, which is extracted from the RF echo signal filtered with the determined cutoff frequency, is used as the feature for classification by the EM algorithm.

5. In vivo Experimental Results

Figure 6(a) shows the manually assigned regions used for adaptive determination of the frequency response of the MTI filter based on echo amplitudes in the assigned regions. These regions were also used to determine the initial parameters of the EM algorithm for segmentation.[20] Figures 6(b) and 6(c) respectively show histograms of the echo amplitude in the regions assigned in the heart wall and lumen shown in Fig. 6(a). As shown in Figs. 6(b) and 6(c), the amplitudes of echoes from the lumen were much less than that of echoes from the heart wall. Thus, the lower limit amplitude e_1 was set to $e_{exp,1}$ and, as shown in Fig. 6(d), the candidate points (colored in red) of the heart wall were successfully extracted from the heart wall.

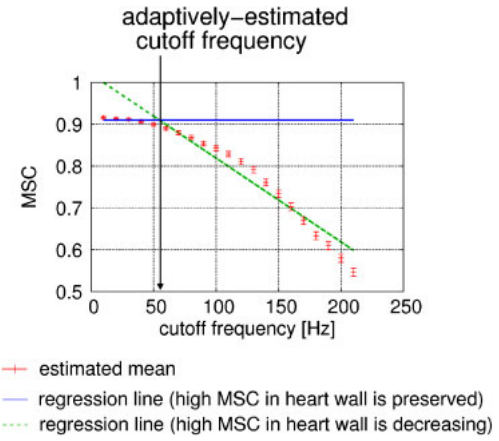

Fig. 7. (Color online) Spatial means of MSCs at candidate points shown in Fig. 6(d) plotted as a function of cutoff frequency of MTI filter and two regression lines at the minimum total error.

Figure 7 shows the spatial means of the MSC at the candidate points shown in Fig. 6(d) at different cutoff frequencies of the MTI filter and the two regression lines with the minimum total error E. The plots and vertical bars show the means $\mu(f_p(i))$ and twice the values of the standard errors of the means $\varepsilon(f_p(i))$, respectively. The cutoff frequency of the MTI filter was adaptively set at 55 Hz at which the two regression lines intersect. Figures 8(a)–8(c) show the MSC image obtained with the previously determined MTI filter, whose cutoff frequency is set at 10 Hz, region-identified image, and the region-identified image overlaid on the corresponding B-mode image, respectively. Figures 8(d)–8(f) show the MSC image with the adaptive MTI filter, whose cutoff frequency is

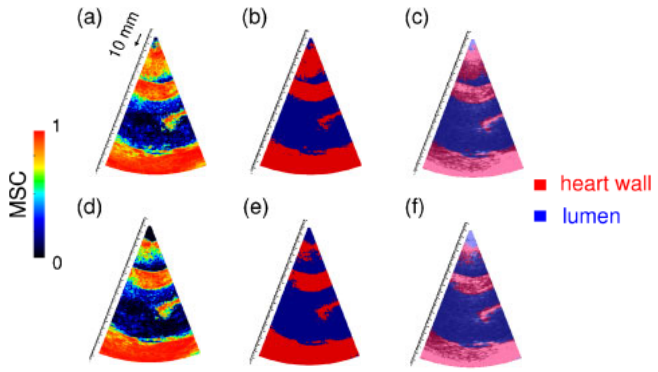

Fig. 8. (Color online) (a) MSC image obtained with previously determined MTI filter whose cutoff frequency is set at 10 Hz, (b) region-identified image, and (c) region-identified image overlaid on the corresponding B-mode image. (d) MSC image obtained with adaptive MTI filter whose cutoff frequency was automatically set at 55 Hz, (e) region-identified image, and (f) region-identified image overlaid on the corresponding B-mode image.

automatically set at 55 Hz, the region-identified image, and the region-identified image overlaid on the corresponding B-mode image, respectively. By comparing Figs. 8(a) and 8(b) with Figs. 8(d) and 8(e), the number of points in the RV showing high MSCs was significantly reduced and these points were correctly classified as the lumen using the adaptive MTI filter.

6. Discussion

As shown in Sect. 5, the amplitude of the echo signal from the IVS was used to assign candidate points of the heart wall and determine the cutoff frequency of the MTI filter for the MSC. In the LV in the longitudinal axis view, the amplitude of the echo from the LV-PW, should be lower than that from the IVS owing to the larger propagation loss. Thus, the selected candidate points depend on the location of the region which is assigned as the heart wall. We investigated the effect of a difference in assigned regions. Figures 9(a) and 9(b) show manually assigned regions and histograms of the echo amplitudes in the region assigned in the LV-PW, respectively. As shown by the fitted Rayleigh distributions in Fig. 9(b), the amplitudes of echoes from the LV-PW were lower than that of echoes from the IVS. Figure 9(c) shows the candidate points of the heart wall extracted on the basis

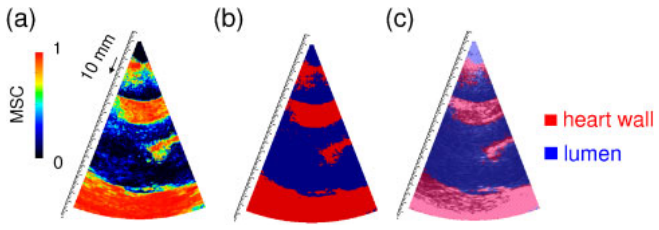

Fig. 10. (Color online) (a) MSC image obtained with adaptive MTI filter whose cutoff frequency was automatically set at 62 Hz, (b) region-identified image, and (c) region-identified image overlaid on the corresponding B-mode image using candidate points extracted on the basis of echo amplitudes in LV-PW.

of the echo amplitudes in the region assigned in the LV-PW. By comparing Fig. 6(d) with Fig. 9(c), the selected candidate points for the heart wall are found to be in the region assigned as the heart wall. Most of the candidate points for the heart wall, however, were assigned in the heart wall region for these two different assignments. Figures 10(a)–10(c) show the MSC image obtained with the adaptive MTI filter whose cutoff frequency is adaptively set to 62 Hz using candidate points for the heart wall shown in Fig. 9(c), the region-identified image, and the region-identified image overlaid on the corresponding B-mode image, respectively. As shown in Fig. 10, the number of points with high MSCs in the RV was reduced and these points were correctly classified as the lumen using the proposed adaptive MTI filter. This result indicates that the effect of the proposed adaptive MTI filter hardly depends on the location of the manually assigned region.

In the present study, high-frame-rate echocardiographic measurement by parallel beamforming with plane wave transmission was used to increase the MSCs of RF echo signals in kernels, which traced the motion of tissue using the phased tracking method, in the heart wall. Furthermore, the high-frame-rate measurement is needed to selectively suppress the clutter component without decreasing the echo from the myocardium as a result of MTI filtering. Figure 11(b) shows spatially averaged power spectra which were obtained by applying a DFT with respect to the direction of the frame to the RF echo signals from the IVS and LV-PW assigned in Fig. 11(a) at the beginning of the slow filling phase. The RF echo signals were obtained at a

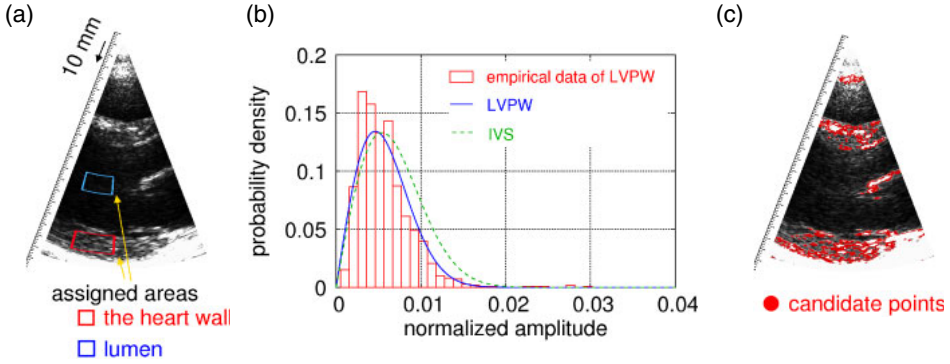

Fig. 9. (Color online) (a) Regions manually assigned for determination of frequency response of MTI filter and initial parameters of EM algorithm. (b) Histograms of echo amplitudes in the regions assigned in LV-PW shown in (a), fitted Rayleigh distribution (blue line) and that shown in Fig. 6(b) (green line). (c) Candidate points for the heart wall extracted on the basis of echo amplitudes in the assigned regions.

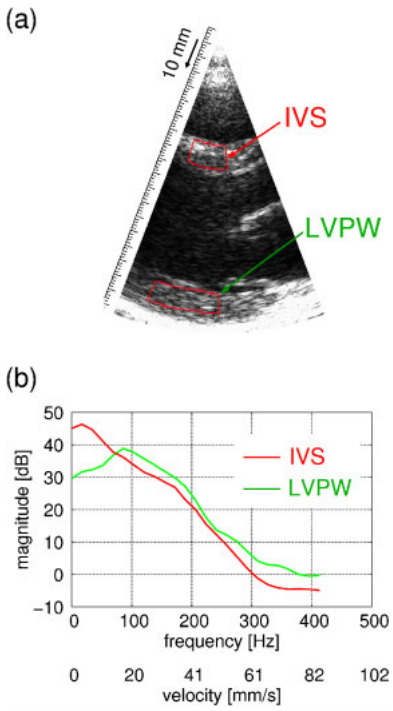

Fig. 11. (Color online) (a) Regions manually assigned in IVS and LVPW at the beginning of the slow filling phase and (b) power spectra spatially averaged in regions assigned in (a).

very high frame rate of 860 Hz by parallel beamforming. As shown in Fig. 11(b), RF echoes from the myocardia contained the dominant frequency component, which was up to at least 100 Hz. The frame rate, however, is about 100 Hz by conventional beamforming and, thus, aliasing of the estimated myocardial velocities occurs for velocity components above the Nyquist limit corresponding to half of the frame rate. The MSCs of echoes from the myocardia should be decreased by MTI filtering because MTI filtering reduces not only the stationary clutter components but echoes from the myocardia, which contain aliased velocity components. Therefore, high-frame-rate measurement is desirable to suppress the clutter component without decreasing the myocardium component by MTI filtering. On the other hand, the sidelobe level in parallel beamforming with plane wave transmission is higher than that in conventional beamforming because the transmitted ultrasound wave is unfocused for high-frame-rate measurement with parallel beamforming. Therefore, as compared to conventional beamforming, parallel beamforming with plane wave transmission increases the clutter component, which includes echoes reflected from the ribcage and the nearby myocardium caused by the sidelobe. The proposed method reduces the effect of the clutter component, which is increased by parallel beamforming with the transmission of an unfocused wide beam.

7. Conclusions

In this study, we investigated the source of clutter, which increases the MSC in the cardiac lumen, and proposed a method for suppressing the increase in the MSC in the lumen caused by the clutter by adaptive determination of the frequency response of an MTI filter applied to the echo signals before estimating the MSCs. According to the results of our investigation shown in Fig. 4, the source of the clutter, which increases the MSC in cardiac lumens, is reverberation and off-axis echo from adjacent myocardia in addition to extra cardiac structures such as ribs and lungs. As compared to with a previous method for automated identification of the heart wall,[20] the heart wall regions were more accurately identified using our proposed method. Furthermore, the result shows the feasibility of identification of the RV-AW which should be observed to diagnose pulmonary embolism and pulmonary hypertension.

1) G. R. Sutherland, M. J. Stewart, K. W. Groundstroem, C. M. Moran, A. Fleming, F. J. Guell-Peris, R. A. Riemersma, L. N. Fenn, K. A. Fox, and W. N. McDicken: J. Am. Soc. Echocardiogr. **7** (1994) 441.
2) G. R. Sutherland, G. D. Salvo, P. Claus, J. D'hooge, and B. Bijnens: J. Am. Soc. Echocardiogr. **17** (2004) 788.
3) A. Heimdal, A. Støylen, H. Torp, and T. Skjræpe: J. Am. Soc. Echocardiogr. **11** (1998) 1013.
4) W. N. McDicken, G. R. Sutherland, C. M. Moran, and L. N. Gordon: Ultrasound Med. Biol. **18** (1992) 651.
5) L. N. Bohs, B. J. Geinman, M. E. Anderson, S. C. Gebhart, and G. E. Trahey: Ultrasonics **38** (2000) 369.
6) J. D'hooge, E. Konofagou, F. Jamal, A. Heimdal, L. Barrios, B. Bijnens, J. Theoen, F. V. de Werf, G. R. Sutherland, and P. Suetens: IEEE Trans. Ultrason. Ferroelectr. Freq. Control **49** (2002) 281.
7) Y. Honjo, H. Hasegawa, and H. Kanai: Jpn. J. Appl. Phys. **51** (2012) 07GF06.
8) D. S. Bach, W. F. Armstrong, C. L. Donovan, and D. W. M. Muller: Am. Heart J. **132** (1996) 721.
9) T. Edvardsen, S. Aakhus, K. Endresen, R. Bjomerheim, O. A. Smiseth, and H. Ihlen: J. Am. Soc. Echocardiogr. **13** (2000) 986.
10) F. Jamal, T. Kukulski, G. R. Sutherland, F. Weidemann, J. D'hooge, B. Bijnens, and G. Derumeaux: J. Am. Soc. Echocardiogr. **15** (2002) 723.
11) J. U. Voigt, G. Lindenmeier, B. Exner, M. Regenfus, D. Werner, U. Reulbach, U. Nixdorff, F. A. Flachskampf, and W. G. Daniel: J. Am. Soc. Echocardiogr. **16** (2003) 415.
12) H. Shida, H. Hasegawa, and H. Kanai: Jpn. J. Appl. Phys. **51** (2012) 07GF05.
13) H. Kanai: Ultrasound Med. Biol. **35** (2009) 936.
14) H. Kanai and M. Tanaka: Jpn. J. Appl. Phys. **50** (2011) 07HA01.
15) E. Konofagou and J. Provost: J. Biomech. **45** (2012) 856.
16) S. G. Lacerda, A. F. da Rocha, D. F. Vasconcelos, J. L. A. de Carvalho, I. G. Sene, Jr., and J. F. Camapum: Conf. Proc. IEEE Engineering in Medicine and Biology Society, 2008, p. 222.
17) M. Marsousi, J. Alirezaie, A. Ahmadian, and A. Kocharian: Conf. Proc. IEEE Engineering in Medicine and Biology Society, 2010, p. 3125.
18) M. M. Nillesen, R. G. P. Lopata, I. H. Gerrits, H. J. Huisman, J. M. Thijssen, L. Kapusta, and C. L. de Korte: Proc. IEEE Int. Symp. Biomedical Imaging: From Nano to Macro, 2009, p. 522.
19) M. M. Nillesen, R. G. P. Lopata, H. J. Huisman, J. M. Thijssen, L. Kapusta, and C. L. de Korte: Ultrasound Med. Biol. **37** (2011) 1409.
20) H. Takahashi, H. Hasegawa, and H. Kanai: Jpn. J. Appl. Phys. **50** (2011) 07HF16.
21) G. Zwirn and S. Akselrod: Ultrasound Med. Biol. **32** (2006) 43.
22) T. Kinugawa, H. Hasegawa, and H. Kanai: Jpn. J. Appl. Phys. **47** (2008) 4155.
23) B. R. Mahafza: *Introduction to Rader Analysis* (CRC Press, Boca Raton, FL, 1998).
24) H. Kanai, M. Sato, Y. Koiwa, and N. Chubachi: IEEE Trans. Ultrason. Ferroelectr. Freq. Control **43** (1996) 791.
25) M. Tanter, J. Bercoff, L. Sandrin, and M. Fink: IEEE Trans. Ultrason. Ferroelectr. Freq. Control **49** (2002) 1363.
26) H. Hasegawa and H. Kanai: IEEE Trans. Ultrason. Ferroelectr. Freq. Control **55** (2008) 2626.
27) H. Hasegawa and H. Kanai: J. Med. Ultrason. **38** (2011) 129.
28) A. P. Dempster, N. M. Laird, and D. B. Rubin: J. R. Stat. Soc., Ser. B **39** (1977) 1.
29) M. A. Lediju, B. C. Byram, and G. E. Trahey: Proc. IEEE Int. Ultrasonics Symp., 2009, p. 1419.